Evidence for Changes in Arctic Cloud Phase Due to Long-Range Pollution Transport

Quentin Coopman, J. Riedi, D. Finch, T. J. Garrett

AGU100 ADVANCING EARTH AND SPACE SCIENCE

Geophysical Research Letters

RESEARCH LETTER
10.1029/2018GL079873

Key Points:
- MODIS and POLDER-3 can be used to provide space-based measurements of phase transitions in liquid arctic clouds
- A smaller droplet effective radius is associated with an increase in the amount of supercooling required for freezing
- Anthropogenic pollution plumes are associated with a decrease in the amount of supercooling required for freezing

Supporting Information:
- Supporting Information S1

Correspondence to:
Q. Coopman,
quentin.coopman@kit.edu

Citation:
Coopman, Q., Riedi, J., Finch, D. P., & Garrett, T. J. (2018). Evidence for changes in arctic cloud phase due to long-range pollution transport. *Geophysical Research Letters*, *45*, 10,709–10,718. https://doi.org/10.1029/2018GL079873

Received 23 FEB 2018
Accepted 18 SEP 2018
Accepted article online 21 SEP 2018
Published online 10 OCT 2018

Evidence for Changes in Arctic Cloud Phase Due to Long-Range Pollution Transport

Q. Coopman[1,2,3], J. Riedi[1], D. P. Finch[4], and T. J. Garrett[2]

[1]Université de Lille, CNRS, UMR 8518-LOA-Laboratoire d'Optique Atmosphérique, Lille, France, [2]Department of Atmospheric Sciences, University of Utah, Salt Lake City, UT, USA, [3]Now at Institute of Meteorology and Climate Research, Karlsruhe Institute of Technology, Karlsruhe, Germany, [4]School of Geoscience, University of Edinburgh, Edinburgh, UK

Abstract Reduced precipitation rates allow pollution within air parcels from midlatitudes to reach the Arctic without being scavenged. We use satellite and tracer transport model data sets to evaluate the degree of supercooling required for 50% of a chosen ensemble of low-level clouds to be in the ice phase for a given meteorological regime. Our results suggest that smaller cloud droplet effective radii are related to higher required amounts of supercooling but that, overall, pollution plumes from fossil fuel combustion lower the degree of supercooling that is required for freezing by approximately 4 °C. The relationship between anthropogenic plumes and the freezing transition temperature from liquid to ice remains to be explained.

Plain Language Summary Anthropogenic pollution plumes from midlatitudes can be transported long distances to the Arctic. In this study, we analyze the impact of these plumes on how easily liquid clouds over the Arctic Ocean freeze by using a novel combination of satellite measurements and a pollution transport model. We find that liquid clouds in polluted air switch phase to become ice clouds at temperatures that are 4 °C higher they would otherwise in pristine air. Because ice clouds in the Arctic precipitate more easily than liquid clouds, the potential is that distant industrial pollution sources are acting to reduce arctic cloud life time.

1. Introduction

In the Arctic, climate change is both more intense and more uncertain than at midlatitudes (Boucher et al., 2013; Stephens, 2005). Cloud phase transitions play a key role in how clouds affect the arctic surface radiation balance (Choi et al., 2014; Curry et al., 1996; Garrett et al., 2009; Kay & L'Ecuyer, 2013; Komurcu et al., 2014; Zamora et al., 2018). Ice nuclei can limit cloud lifetime by triggering frozen precipitation as snow and ice clouds tend to be less optically and thermally opaque.

Measurements of ice nucleation rates from laboratory and field studies made over the past two decades can differ by orders of magnitude (Jeffery & Austin, 1997; Pruppacher, 1995) making it difficult to bring ice nucleation theory into agreement with observations (Doutriaux-Boucher & Quaas, 2004). As background, the ice nucleation rate (J) is defined by (Lamb & Verlinde, 2011)

$$J = K_X \exp\left(-\frac{\Delta G^*}{k_b T}\right) \tag{1}$$

with K_X a thermodynamic constant, k_b the Boltzmann constant, T the temperature of the system, and ΔG^* is the energy barrier from liquid to ice transition. ΔG^* for heterogeneous nucleation can be expressed as

$$\Delta G^* = \frac{16\pi\sigma_{lL}^3}{3(n_l \Delta\mu_{Ll})^2} \cdot f \tag{2}$$

where n_l is the molar density of ice, $\Delta\mu_{Ll}$ is the chemical potential of bulk liquid parent phase relative to ice, σ_{Ll} is the interfacial free energy between the solid and the liquid phase, and f is related to a geometrical factor.

The supercooling temperature ΔT can be related to the chemical potential through $\Delta\mu_{Ll} = l_{Ll}\Delta T/T_0$ where T_0 is the melting temperature and l_{Ll} is the latent heat of freezing. Then, equation (2) becomes

$$\Delta G^* = \frac{f'}{\Delta T^2} \tag{3}$$

where f' expresses the parameters that are not dependent on ΔT. If ΔT is greater than or equal to the supercooling freezing temperature ΔT^*, the energy barrier for freezing has been crossed.

The arctic atmosphere is remote from major pollution sources, but it is not necessarily pristine (Marelle et al., 2015; Shaw, 1995). Low precipitation rates during winter and early spring allow pollution plumes from midlatitudes to reach the Arctic without scavenging en route (Garrett et al., 2010; Stohl et al., 2007). Coopman et al. (2016) and Coopman et al. (2017) showed that pollution plumes from fossil fuel combustion interact with liquid arctic clouds and are associated with smaller cloud droplet effective radii. Pollution plumes from biomass burning have a weaker impact, mostly due to typically unfavorable conditions for cloud formation (Monks et al., 2012) at the plume source (Martin et al., 2013). Other sources can also emit potential ice nuclei, such as desert dust (Murray et al., 2012; Prenni et al., 2012).

In the present study, we focus on the effect of pollution plumes from anthropogenic sources on cloud phase transitions in the Arctic. Specifically, we investigate the relationship between ΔT^* and aerosols by colocating cloud microphysical properties from space-spaced sensors with a passive tracer of aerosol from a numerical tracer transport model. Aerosols have the potential to affect cloud properties, such as cloud droplet size and cloud phase, and thereby alter cloud precipitation rates, in which case through scavenging they affect their own concentrations. For the purpose of studying interactions between pollution plumes and distant clouds, use of carbon monoxide (CO) as a pollution tracer has helped with robust attribution. CO is a by-product of incomplete combustion, and CO variations correlate well with aerosols close to industrial sources in nonprecipitating air parcels (Garrett & Zhao, 2006; Longley et al., 2005). Previous studies have shown that CO is highly correlated with aerosols in arctic pollution plumes (Paris et al., 2009; Stohl et al., 2007; Warneke et al., 2009), although the relationship is frequently decoupled in summer when precipitation along transport pathways is high (Garrett et al., 2011). If aerosol and CO concentrations become decoupled downstream from pollution sources due to, for example, wet scavenging, then aerosols cannot reach the arctic region and air from aerosol source regions should not be expected to impact cloud phase transitions. CO has previously been used as aerosol tracer to study aerosol-cloud interactions (Avey et al., 2007; Brioude et al., 2009; Coopman et al., 2017, 2016; Garrett & Zhao, 2006; Garrett et al., 2010; Tietze et al., 2011; Yang et al., 2015; Zamora et al., 2016). Colocating a passive tracer of aerosol, such as CO, from a tracer transport numerical model with cloud microphysical parameters from satellite instruments allows for the study of aerosol impacts on cloud properties from two independent and decoupled data sets (Tietze et al., 2011).

2. Data

Cloud properties are obtained from the spaced-based sensors Moderate-Resolution Imaging Spectroradiometer (MODIS; Platnick et al., 2003) and POLarization and Directionality of the Earth's Reflectance (POLDER; Bréon & Colzy, 1999), both part of the A-train mission. POLDER-3 camera captures spectral, directional, and polarized measurements of reflected sunlight through a wide field of view (Fougnie et al., 2007). POLDER-3 cloud microphysical properties retrievals have a 36-km × 36-km spatial resolution. The MODIS instrument provides observations in 36 different spectral bands with central wavelength from 400 to 14,400 nm. The pixel resolution of the retrievals at nadir is 1 km × 1 km for cloud microphysical properties and 5 km × 5 km for cloud top temperature and pixel sizes increase toward swath edges. We use Collection 6 Level 2 products from MODIS (Platnick et al., 2014): cloud optical depth (τ), cloud droplet effective radius (r_e), and cloud top temperature. The uncertainty in cloud microphysical parameters from MODIS depends on surface type, solar/view geometry, atmospheric state, surface and cloud temperature, and where the solution lies in the τ-r_e space (Platnick et al., 2004, 2014; Sun et al., 2012). The uncertainty in r_e^{Liq} for the data points used in this study is (Hubanks et al., 2018): 75% of our data points have an uncertainty in r_e^{Liq} less than 30%, and 50% of the data points have an uncertainty less than 10%—see Figures S5 and S6 and Text S4 in the supporting information.

POLDER cloud top pressure retrievals are based on measurements in the oxygen A-band (Bréon & Colzy, 1999). They are more sensitive to the presence of low-level clouds (Tietze et al., 2011) than MODIS retrievals that are based on cloud brightness temperature (Platnick et al., 2014). We avoid cases of multilayered clouds, frequently occurring in the Arctic (Liu et al., 2012), by considering only cloudy pixels for which cloud top pressures (CTPs) from the two instruments differ by less than 200 hPa (Desmons et al., 2017). Then, CTP from POLDER-3 rather than MODIS is used because POLDER CTP gives a retrieval that is not impacted by surface temperature inversions that are particularly frequent in the Arctic (Tietze et al., 2011).

To determine cloud thermodynamic phase, we use an algorithm that takes advantage of multiangle polarization, shortwave, thermal infrared, and visible measurements from both POLDER and MODIS to retrieve a thermodynamic phase index between 0 for liquid clouds and 200 for ice clouds (Riedi et al., 2010). A pixel with an index less than 60 is considered to be confidently liquid and a pixel with an index greater than 140 is considered to be confidently ice (Coopman et al., 2016).

We colocate vertically, horizontally, and temporally cloud data from POLDER and MODIS with meteorological parameters from ERA-Interim reanalyses (Berrisford et al., 2011) from European Centre for Medium-Range Weather Forecasts, in particular lower tropospheric stability (LTS) and specific humidity (SH).

Aerosol content is inferred from model CO concentrations, taken as a passive tracer of aerosols from the numerical tracer transport model GEOS-Chem (Goddard Earth Observing System). In the model, CO has no sink such as oxidation processes. We use the version v9-01-03 of GEOS-Chem (Bey et al., 2001). The model is described extensively by Parrington et al. (2012) and Finch et al. (2014). The CO is *tagged* in the numerical model according to biomass burning and anthropogenic sources. The model is run at a spatial resolution of 2° in latitude and 2.5° in longitude at 47 native vertical levels to track concentrations of pollution downwind of source regions. The model considers three CO sources: fossil fuel emissions from the Emission Data set for Global Atmospheric Research (Olivier et al., 1999), the Big Bend Regional Aerosol and Visibility Observational (Kuhns et al., 2005), the European Monitoring and Evaluation Programme (Vestreng & Klein, 2002), and STREETS (Streets et al., 2003); second, BB emissions from the Global Fire Emissions Database (Giglio et al., 2010); and third, biogenic emissions from the Model of Emissions of Gases and Aerosol from Nature (Guenther et al., 2006). Since we focus only on anthropogenic pollution effects, only GEOS-Chem bins with fossil fuel combustion sources representing more than two thirds of CO from combustion sources are considered.

The model capabilities have been discussed by Bey et al. (2001), Fisher et al. (2010), Parrington et al. (2012), Finch et al. (2014), and Mackie et al. (2016). Finch et al. (2014) compared CO from field campaigns and from GEOS-Chem and found a Spearman's rank correlation of 0.65. Coopman et al. (2017) performed a linear fit between modeled CO and measured CO from five Arctic stations and retrieved a slope of 0.8 with correlation coefficients greater than 0.68. Monks et al. (2015) compared 11 atmospheric models with chemistry and evaluated the simulated CO concentration in the Arctic: They concluded that CO concentration (χ_{CO}) retrieved by GEOS-Chem showed better agreements with observations than χ_{CO} retrieved from other models.

Thermodynamic phase transitions from liquid to ice clouds can be favored by the presence of desert dust (DeMott et al., 2003; Myhre et al., 2007; Smoydzin et al., 2012; Xie, 1999). To obtain only the effects of fossil fuel combustion aerosols, we discard pixels for which desert dust aerosol optical depth represents more than 20% of the total aerosol optical depth, represented by the sum of desert dust, sea salt, organic matter, black carbon, and sulfate obtained from Monitoring Atmospheric Composition and Climate reanalyses from European Centre for Medium-Range Weather Forecasts (Benedictow et al., 2014; Stein et al., 2011). We tested the sensitivity to using different thresholds with respect to the aerosol optical depth of dust at 10% and 5% of the total aerosol optical depth. The results are similar to the results presented here—see Text S2 and Figures S1–S3 in the supporting information for details.

In this study, we consider data for the time period between 2005 and 2010, for latitudes higher than 65°N, over the Arctic ocean, MODIS and POLDER are unable to retrieve cloud microphysical properties from measurements at visible wavelengths during the night; therefore, our analysis is limited to the period between March and September. In order to obtain grid cells of constant areas at every latitude, we project all data onto a sinusoidal grid with an equivalent resolution at the equator of 54 km × 54 km. One grid cell may comprise up to 81 satellite pixels. In this study, we only consider grid cells for which more than 80% of the pixels are liquid or more than 80% of pixels are ice. Details about the colocalization technique can be found in Coopman et al. (2016) and Coopman et al. (2017).

3. Method

Meteorological parameters, such as atmospheric stability and humidity, are the primary factors that affect cloud microphysical properties (Andersen et al., 2015; Chen et al., 2014; Garrett & Zhao, 2006) and any correlation or anticorrelation of meteorological parameters with pollution plumes can inhibit or augment any apparent aerosol-cloud interactions in the Arctic (Coopman et al., 2017, 2016). An aerosol-cloud interaction parameter (*ACI*) has been defined by Feingold et al. (2001) that represents the relative variation of cloud microphysical parameters with associated variations in CCN. Coopman et al. (2016) used CO as a passive tracer of

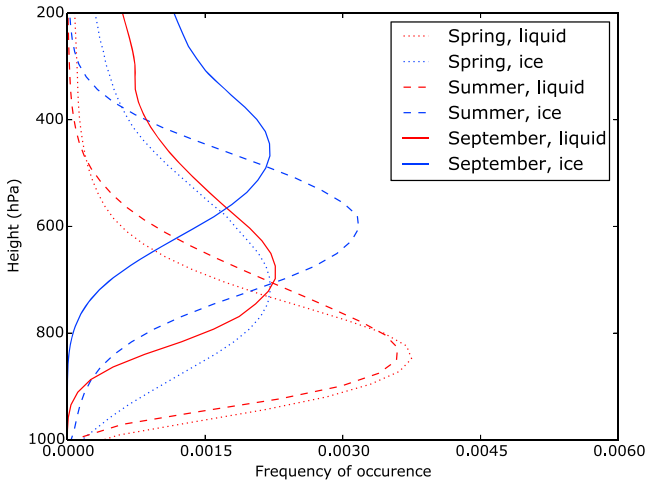

Figure 1. Normalized distributions of liquid- (red) and ice-cloud (blue) top pressure for different seasons from March 2005 to September 2010 above the arctic circle from POLarization and Directionality of the Earth's Reflectance 3 cloud top pressure.

CCN and showed that for SH below 1 g/kg there is no correlation between CO and r_e, finding a value for *ACI* close to 0, whereas for SH greater than 4 g/kg the *ACI* with respect to the sensitivity of effective radius to CO is close to 14%.

In the present study, in order to control for the correlation between pollution concentration and meteorological parameters, we limit LTS to a range between 15.2 and 22 K and SH from 0.8 to 4 g/kg. These ranges correspond to 15% of the total span of LTS and SH centered at the respective mode of each of their distributions (Coopman et al., 2016). Within this 15% range, the number of data points is sufficiently large, and meteorological parameters sufficiently constrained, that any observed supercooling freezing temperature change can be attributed to changes in pollution concentrations or changes in droplet r_e and not to a coincident correlation between pollution concentrations or droplet effective radii and the local meteorology (Coopman et al., 2017, 2016).

Figure 1 shows the normalized frequency distribution for the CTP of liquid and ice clouds at different times of the year. In spring, summer, and September, liquid-cloud modes of the distribution lie respectively at 945, 943, and 690 hPa. Ice-cloud modes lie at 710, 580, and 440 hPa. Ice CTP is at a lower pressure than liquid CTP. Seasonally, clouds are located at higher pressures in spring. We differentiate clouds with CTP below 800 hPa as high-level clouds, and clouds with CTP greater than 800 hPa as low-level clouds.

We controlled for liquid water path (LWP) in order to isolate possible feedbacks from radiative dynamic effects. Clouds with a LWP less than 40 g/m^2 act as a graybody, and their radiative properties are therefore dependent on their microphysical properties (Garrett et al., 2009). Clouds with LWP exceeding 40 g/m^2 approximate a blackbody, and so the longwave emission is determined by temperature changes alone. The data set is therefore divided into four categories: (i) low LWP and low CTP, (ii) low LWP and high CTP, (iii) high LWP and low CTP, and (iv) high LWP and high CTP.

The main goal of this study is to analyze freezing temperature variations as function of cloud microphysical parameters and pollution plume concentrations. We consider four different regimes for both r_e and χ_{CO} and the four bins are defined by the quartile values: lower, median, and upper. The four bins for r_e are delimited by the following thresholds: 9.4, 11.4, and 13.1 μm; the four bins for χ_{CO} are delimited by the following thresholds: 44, 53, and 75 ppb.

Figure 2 shows the temperature distributions of the tops of liquid and ice clouds. We define ice phase fraction as the number of ice grid cells — i.e., grid cells for which 80% at least of the pixels are ice — divided by the number of liquid and ice grid cells. Using passive space-based instruments, it is difficult to identify mixed-phased clouds with high confidence. Therefore, mixed-phase clouds and clouds for which the degree of confidence in the cloud phase is not high are not considered (Riedi et al., 2010). Ice phase fraction is evaluated as a function of cloud top temperature for the previously defined meteorological parameter regimes — specifically SH and LTS — for four different regimes of pollution content, four regimes of cloud droplet r_e, two regimes of LWP, and two regimes of CTP.

Mathematically speaking, previous work has assumed an exponential function for ice fraction (χ_{Ice}) as a function of supercooling temperature (Del Genio et al., 1996; Hu et al., 2009; Le Treut & Li, 1991). Here a hyperbolic tangent function is used:

$$X_{Ice} = \frac{1 + \tanh(-a_1 \times \Delta T + a_2)}{2} \tag{4}$$

The hyperbolic function gives a one-to-one relationship between χ_{Ice} and temperature and concisely represents observations (Doutriaux-Boucher & Quaas, 2004). We can ensure that the sum of ice and liquid fractions is equal to 100% for each temperature bin. The a_1 parameter controls the flatness of the curve, so that lower absolute values represent a more gradual water-ice transition with respect to temperature. The a_2 parameter controls the temperature at which the χ_{Ice} is equal to 50%. (iii) The parameter a_2/a_1 represents the supercooling temperature for which the ice-cloud fraction is equal to the liquid-cloud fraction (e.g., X_{Ice} = 50%) and is

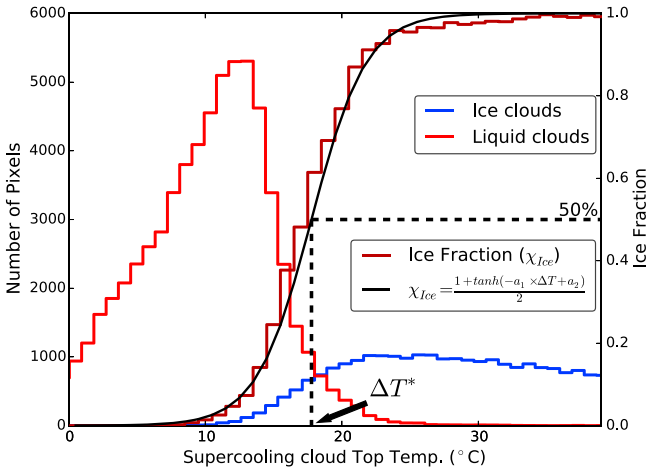

Figure 2. The temperature distribution of the tops of liquid and ice clouds. Ice fraction (χ_{Ice}) as function of the supercooling cloud top temperature with the associated hyperbolic tangential fit presented by equation (4) and the temperature at which the χ_{Ice} is equal to 50%. This temperature is referred to here as the supercooling freezing temperature ΔT^*. The χ_{Ice} is defined as the number of grid cells considered to be ice divided by the number of grid cells considered as either liquid or ice.

considered here as the median freezing temperature:

$$\Delta T_{50} = \frac{a_2}{a_1} \tag{5}$$

from which the uncertainty $\delta\Delta T_{50}$ associated with the uncertainties δa_1 and δa_2 is

$$\delta(\Delta T_{50})^2 = \Delta T_{50}^2 \left(\left(\frac{\delta a_2}{a_2} \right)^2 + \left(\frac{\delta a_1}{a_1} \right)^2 \right) \tag{6}$$

In this manner, the use of an hyperbolic fitting function simplifies study of liquid-solid water transitions in arctic clouds as a function of meteorological and pollution plume regime.

Figure 2 shows an example of the χ_{Ice} as a function of supercooling temperature fitted to the hyperbolic tangential curve of equation (4). The observed curves reach an χ_{Ice} of 0 below 0 °C and 1 above 40 °C, consistent with classical ice nucleation theory. The supercooling temperature at which the χ_{Ice} is equal to 50% is considered to be ΔT^*.

4. Results

Figure 3 shows the supercooling freezing temperature (ΔT^*), calculated from space-based observations, for four liquid-cloud-droplet r_e regimes and for the four different cloud types. χ_{Ice} is determined from the combined liquid and ice cloud top temperature distributions. Only liquid cloud top temperature distributions are binned for cloud droplet r_e regimes. For example, ΔT^* for low LWP and low CTP clouds is 13.8 °C for values of liquid-cloud r_e smaller than 9.4 µm. It drops to 11.4 °C for values of liquid-cloud r_e greater than 13.1 µm. On average, for all cloud types, ΔT^* decreases by 1.0 °C between the lower and upper regimes in r_e, defined by the lower and upper quartile values in r_e.

From Figure 3, clouds with low LWP are associated with lower supercooling freezing temperatures. Average values of ΔT^* are equal to 11.4 °C for LWP values less than 40 g/m^2, compared to 15.5 °C for clouds with LWP

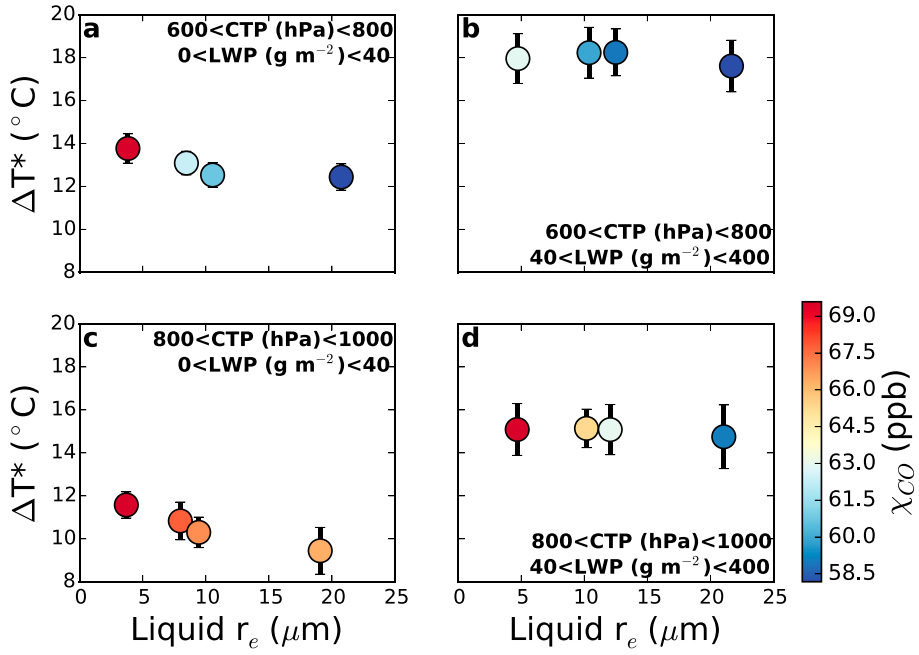

Figure 3. Supercooling freezing temperature (ΔT^*) as a function of the liquid-cloud-droplet effective radius (r_e) for four cloud categories differentiated by their liquid water path (LWP) and cloud top pressure (CTP). The color scale corresponds to the associated mean CO concentration (χ_{CO}). The uncertainty bars are calculated from equation (6).

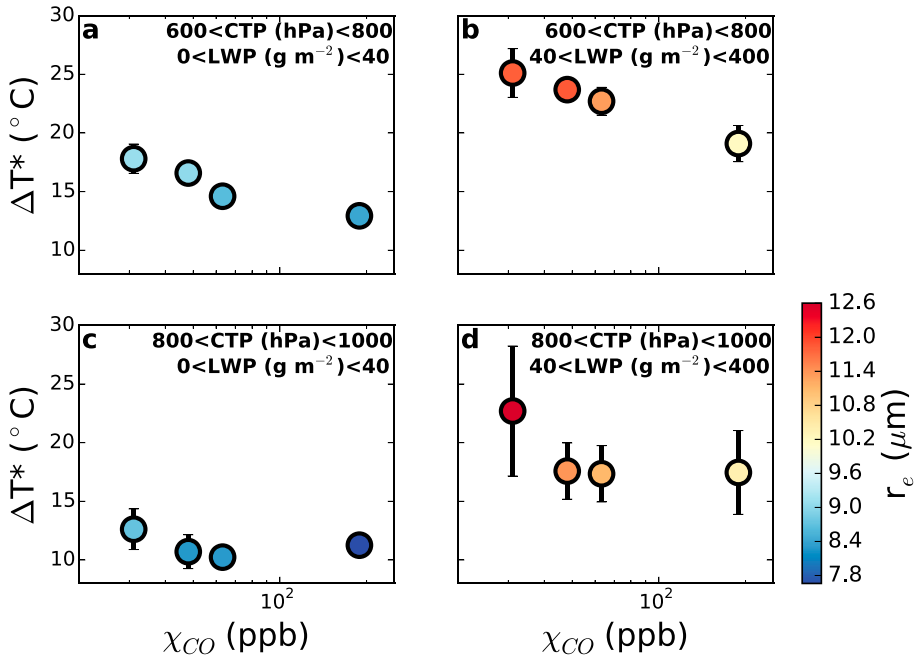

Figure 4. Supercooling freezing temperature (ΔT^*) as a function of the CO concentration (χ_{CO}) for four cloud categories differentiated by their liquid water path (LWP) and cloud top pressure (CTP). The color scale corresponds to the associated mean liquid-cloud droplet effective radius (r_e). The uncertainty bars are calculated from equation (6).

values greater than 40 g/m^2. One possible explanation for this difference is that if clouds are optically thin, the surface can increase the retrieved brightness temperature of the cloud (Platnick et al., 2003) and artificially decrease the derived value of ΔT^*. We observe that there is not a strong dependence of ΔT^* on r_e for LWP greater than 40 g/m^2. For example, ΔT^* is 0.6 °C lower for clouds with $r_e < 9.4$ than for clouds with $r_e > 13.1$ for clouds with low CTP and high LWP, whereas the decrease in ΔT^* is 2.1 °C for the case of clouds with low CTP and low LWP. We hypothesize that clouds with high LWP are more prone to convection and therefore ΔT^* is more likely to be determined by dynamical than microphysical processes. Then, r_e variations do not change the glaciation temperatures for high LWP clouds.

In order to separate a relationship between χ_{CO} and ΔT^* from a relationship between r_e and ΔT^* (e.g., Figure 3), where χ_{CO} is expected to correlate with lower r_e (Coopman et al., 2016, 2017; Tietze et al., 2011), Figure 4 shows ΔT^* for the four χ_{CO} regimes defined by the lower, median, and upper boundaries: 44, 53, and 75 ppb. For each cloud category, ΔT^* decreases with increasing values of χ_{CO}. For example, ΔT^* for clouds with low LWP and CTP is 17.8 °C for χ_{CO} below 44 ppb and 12.9 °C for χ_{CO} greater than 75 ppb. On average, for all cloud categories, ΔT^* decreases by 4.3 °C between the lower and upper quartiles in χ_{CO}. For clouds with low LWP and CTP, the mean r_e decreases from 9.1 μm for χ_{CO} below 44 ppb to 8.4 μm for χ_{CO} greater than 75 ppb. Pollution plumes associated with higher χ_{CO} are associated with faster phase transitions—see Text S3 and Figure S4 in the supporting information for details. Similar decreases in ΔT^* are observed for the other cloud categories.

Unlike r_e, χ_{CO} is related to ΔT^* for values of LWP greater than 40 g/m^2. Assuming that higher values of LWP tend to be associated with a lower stability of the atmosphere, we hypothesize that such conditions are more favorable for the mixing of aerosols into clouds (Andersen et al., 2015; Chen et al., 2014).

In Figure 3, the difference in ΔT^* between the upper and lower quartile regimes in r_e is 1.0 °C, lower than the difference in ΔT^* between the corresponding χ_{CO} regimes (−4.3 °C) shown in Figure 4. This implies that the effect of pollution on cloud glaciation temperature is much more important than the effect of cloud droplet size.

5. Discussion

From aircraft observations of high ice particle concentrations in moderately supercooled arctic clouds, Rangno and Hobbs (2001) hypothesized that ice concentrations can be enhanced by the fragmentation and

Table 1
Ratio of the Free Energy Barrier Height of the Thermodynamic Phase Transition Between Polluted (ΔG_p^*) and Clean (ΔG_c^*) Clouds for Four Cloud Categories Differentiated by Their Liquid Water Path (LWP) and Cloud Top Pressure

Parameters	Low CTP, low LWP	High CTP, low LWP	Low CTP, high LWP	High CTP, high LWP
ΔT_c^* (°C)	17.8	12.4	25.0	22.7
ΔT_p^* (°C)	12.9	11.3	19.1	17.4
$\Delta G_p^*/\Delta G_c^*$	0.53	0.83	0.58	0.59

Note. The ratio is inferred from the ratio of supercooling freezing temperature between polluted (ΔT_p^*) and clean clouds (ΔT_c^*) from Figure 4 and equation (7).

shattering of drops during freezing in free fall. They suggested that cloud tops with large liquid droplets ($r_e > 10$ μm) at temperatures between −20 and −10 °C are characterized by ice concentrations greater than observed ice nuclei concentrations due to the fragmentation of ice crystals. Using satellite measurements, Rosenfeld et al. (2011) showed that the glaciation temperature of clouds increases from −30 to −15 °C when the liquid cloud droplet r_e at −5 °C increases from 4 to 17 μm. Figure 3 shows that, on average, for the four cloud types, the glaciation temperature of clouds increases from −14.6 to −13.4 °C when the liquid cloud droplet r_e increases from 4 to 19 μm. Our results are in line with Rangno and Hobbs (2001) and Rosenfeld et al. (2011) and suggest that clouds associated with larger liquid cloud droplet r_e freeze at warmer temperature than clouds with smaller cloud droplets; large cloud droplets are more likely to support secondary ice nucleation (Mossop, 1976; Rosenfeld et al., 2011).

Figure 3 shows that clouds with small liquid droplet effective radii are associated with an increase in the degree of supercooling that is required for 50% of cloud grid cells to be in the ice phase. We also see that Figure 4 suggests that an increase in pollution concentrations decreases the required degree of supercooling. Thus, our results show two different effects: The first, from Figure 3, is that the required supercooling for freezing decreases when cloud droplet effective radii are large. Since the presence of anthropogenic pollution plumes decreases liquid cloud droplet r_e (Coopman et al., 2017, 2016), from the first effect alone, we would expect that the presence of anthropogenic pollution increases ΔT^*. However, there is a second effect shown in Figure 4, which is that anthropogenic pollution decreases ΔT^*. The two effects may seem contradictory, but our interpretation is that they instead suggest that the association of increased pollution with lower ΔT^* is more important than the respective association with decreased liquid cloud r_e.

With regard to the thermodynamics, from equation (3), the free-energy barrier ΔG^* for formation of an ice embryo from the liquid phase can be related to $1/\Delta T^{*2}$ (e.g., Pruppacher & Klett, 2010, equation (7.37)). Assuming that ΔT_{50} serves as a proxy for ΔT^*, we can link the ratio of free barrier energy heights with the ratio of the retrieved ΔT_{50} (see Text S1 in the supporting information for details):

$$\frac{\Delta G_p^*}{\Delta G_c^*} = \left(\frac{\Delta T_p^*}{\Delta T_c^*}\right)^2 \tag{7}$$

where the subscripts p and c refer, respectively, to polluted and clean clouds. Table 1 shows the ratios of energies between the upper regime in χ_{CO} (e.g., χ_{CO} greater than 75 ppb) and the lower regime in χ_{CO} (e.g., χ_{CO} below 44 ppb), for the four cloud categories in Figure 4. On average, polluted plumes would appear to be associated with a decrease in the free energy barrier ΔG^* of about 37%; there is a decrease of 47% for the low LWP and low CTP regime, and 17% for the low LWP and high CTP regime.

6. Conclusions

We have used space-based observations for quantifying the effect of long-range aerosol transport on arctic cloud phase transitions. Our results show that smaller values of cloud droplet r_e are associated with a greater supercooling required to freeze clouds. However, despite an observed decrease of cloud r_e in polluted air, pollution plumes substantially decrease the degree of required supercooling for glaciation. For a 4.3 °C decrease associated with a shift from χ_{CO} equals 44 ppb to χ_{CO} equals 75 ppb, there is an estimated 37% decrease in the free-energy barrier of the liquid-ice phase transition, implying an increase in the nucleation rate of ice from liquid.

Changes in the free-energy barrier due to increased pollution concentrations may have implications for arctic cloud lifetime by triggering precipitation, and thereby altering cloud radiative properties by making them

thermally and optically less opaque (Morrison et al., 2011; Zamora et al., 2018). Mixed-phase clouds are common in the Arctic (Mioche et al., 2015; Morrison et al., 2011), and their radiative properties play an important role in determining the rate of arctic warming (Cesana et al., 2012; Shupe, 2011; Uchiyama et al., 2014). Nevertheless, our knowledge and understanding remain incomplete (Korolev et al., 2017). Space-based methods for measuring arctic cloud thermodynamics such as those described here may help constrain our understanding of arctic cloud processes on broad spatial and temporal scales.

Acknowledgments
This paper is dedicated posthumously to Kyle Tietze, who developed many of the techniques used in this study while a graduate student at the University of Utah. We thank an anonymous reviewer for constructive comments on the manuscript. The full data set can be found on the NSF Arctic Data Center under the https://doi.org/10.18739/A27C51. This material is based upon work supported by the National Science Foundation under the grant 1303965, the NERC studentship NE/K500835/1, the Pollution in the ARCtic System (PARCS) project, and the University of Lille. The authors thank ICARE/AERIS, NASA, and CNES for the data used in this research.

References

Andersen, H., & Cermak, J. (2015). How thermodynamic environments control stratocumulus microphysics and interactions with aerosols. *Environmental Research Letters*, *10*(2), 024004. https://doi.org/10.1088/1748-9326/10/2/024004

Avey, L., Garrett, T. J., & Stohl, A. (2007). Evaluation of the aerosol indirect effect using satellite, tracer transport model, and aircraft data from the international consortium for atmospheric research on transport and transformation. *Journal of Geophysical Research*, *112*, D10S33. https://doi.org/10.1029/2006JD007581

Benedictow, A., Blechschmidt, A. M., Bouarar, I., Botek, E., Chabrillat, S., Christophe, Y., et al. (2014). Validation report of the MACC reanalysis of global atmospheric composition: Period 2003–2012 (Tech. rep.) MACC–II project Netherlands: KNMI, De Bilt.

Berrisford, P., Dee, D., Fielding, K., Fuentes, M., Kallberg, P., Kobayashi, S., & Uppala, S. (2011). The ERA-Interim archive version 2.0 (Tech. Rep.) UK: ECMWF, Reading.

Bey, I., Jacob, D. J., Yantosca, R. M., Logan, J. a., Field, B. D., Fiore, A. M., et al. (2001). Global modeling of tropospheric chemistry with assimilated meteorology: Model description and evaluation. *Journal of Geophysical Research*, *106*(D19), 23,073–23,095. https://doi.org/10.1029/2001JD000807

Boucher, O., Randall, D., Artaxo, P., Bretherton, C., Feingold, G., Forster, P., et al. (2013). Clouds and aerosols. In Intergovernmental Panel on Climate Change (Ed.), *Climate Change 2013—The Physical Science Basis* (pp. 571–658). Cambridge: Cambridge University Press. https://doi.org/10.1017/CBO9781107415324.016

Bréon, F.-M., & Colzy, S. (1999). Cloud detection from the spaceborne polder instrument and validation against surface synoptic observations. *Journal of Applied Meteorology*, *38*(6), 777–785. https://doi.org/10.1175/1520-0450(1999)038<0777:CDFTSP>2.0.CO;2

Brioude, J., Cooper, O. R., Feingold, G., Trainer, M., Freitas, S. R., Kowal, D., et al. (2009). Effect of biomass burning on marine stratocumulus clouds off the California coast. *Atmospheric Chemistry and Physics*, *9*(22), 8841–8856. https://doi.org/10.5194/acp-9-8841-2009

Cesana, G., Kay, J. E., Chepfer, H., English, J. M., & de Boer, G. (2012). Ubiquitous low-level liquid-containing arctic clouds: New observations and climate model constraints from CALIPSO-GOCCP. *Geophysical Research Letters*, *39*, 6. https://doi.org/10.1029/2012GL053385

Chen, Y.-C., Christensen, M. W., Stephens, G. L., & Seinfeld, J. H. (2014). Satellite-based estimate of global aerosol-cloud radiative forcing by marine warm clouds. *Nature Geoscience*, *7*(9), 643–646. https://doi.org/10.1038/ngeo2214

Choi, Y.-S., Ho, C.-H., Park, C.-E., Storelvmo, T., & Tan, I. (2014). Influence of cloud phase composition on climate feedbacks. *Journal of Geophysical Research: Atmospheres*, *119*, 3687–3700. https://doi.org/10.1002/2013JD020582

Coopman, Q., Garrett, T. J., Finch, D. P., & Riedi, J. (2017). High sensitivity of arctic liquid clouds to long-range anthropogenic aerosol transport. *Geophysical Research Letters*, *45*, 372–381. https://doi.org/10.1002/2017GL075795

Coopman, Q., Garrett, T. J., Riedi, J., Eckhardt, S., & Stohl, A. (2016). Effects of long-range aerosol transport on the microphysical properties of low-level liquid clouds in the arctic. *Atmospheric Chemistry and Physics*, *16*(7), 4661–4674. https://doi.org/10.5194/acp-16-4661-2016

Curry, J. A., Schramm, J. L., Rossow, W. B., & Randall, D. (1996). Overview of arctic cloud and radiation characteristics. *Journal of Climate*, *9*(8), 1731–1764. https://doi.org/10.1175/1520-0442(1996)009<1731:OOACAR>2.0.CO;2

DeMott, P. J., Sassen, K., Poellot, M. R., Baumgardner, D., Rogers, D. C., Brooks, S. D., et al. (2003). African dust aerosols as atmospheric ice nuclei. *Geophysical Research Letters*, *30*(14), 1732. https://doi.org/10.1029/2003GL017410

Del Genio, A. D., Yao, M.-S., Kovari, W., & Lo, K. K.-W. (1996). A prognostic cloud water parameterization for global climate models. *Journal of Climate*, *9*(2), 270–304. https://doi.org/10.1175/1520-0442(1996)009<0270:APCWPF>2.0.CO;2

Desmons, M., Ferlay, N., Parol, F., Riedi, J., & Thieuleux, F. (2017). A global multilayer cloud identification with POLDER/ PARASOL. *Journal of Applied Meteorology and Climatology*, *56*(4), 1121–1139. https://doi.org/10.1175/JAMC-D-16-0159.1

Doutriaux-Boucher, M., & Quaas, J. (2004). Evaluation of cloud thermodynamic phase parametrizations in the LMDZ GCM by using POLDER satellite data. *Geophysical Research Letters*, *31*, L06126. https://doi.org/10.1029/2003GL019095

Feingold, G., Remer, L. a., Ramaprasad, J., & Kaufman, Y. J. (2001). Analysis of smoke impact on clouds in Brazilian biomass burning regions: An extension of Twomey's approach. *Journal of Geophysical Research*, *106*(D19), 22,907–22,922. https://doi.org/10.1029/2001JD000732

Finch, D. P., Palmer, P. I., & Parrington, M. (2014). Origin, variability and age of biomass burning plumes intercepted during BORTAS-b. *Atmospheric Chemistry and Physics*, *14*(24), 13,789–13,800. https://doi.org/10.5194/acp-14-13789-2014

Fisher, J. A., Jacob, D. J., Purdy, M. T., Kopacz, M., Le Sager, P., Carouge, C., et al. (2010). Source attribution and interannual variability of arctic pollution in spring constrained by aircraft (ARCTAS, ARCPAC) and satellite (AIRS) observations of carbon monoxide. *Atmospheric Chemistry and Physics*, *10*(3), 977–996. https://doi.org/10.5194/acp-10-977-2010

Fougnie, B., Bracco, G., Lafrance, B., Ruffel, C., Hagolle, O., & Tinel, C. (2007). PARASOL In-flight calibration and performance. *Applied Optics*, *46*(22), 5435. https://doi.org/10.1364/AO.46.005435

Garrett, T. J., Brattström, S., Sharma, S., Worthy, D. E. J., & Novelli, P. (2011). The role of scavenging in the seasonal transport of black carbon and sulfate to the arctic. *Geophysical Research Letters*, *38*, L16805. https://doi.org/10.1029/2011GL048221

Garrett, T. J., Maestas, M. M., Krueger, S. K., & Schmidt, C. T. (2009). Acceleration by aerosol of a radiative-thermodynamic cloud feedback influencing Arctic surface warming. *Geophysical Research Letters*, *36*, L19804. https://doi.org/10.1029/2009GL040195

Garrett, T. J., & Zhao, C. (2006). Increased arctic cloud longwave emissivity associated with pollution from mid-latitudes. *Nature*, *440*(7085), 787–789. https://doi.org/10.1038/nature04636

Garrett, T., Zhao, C., & Novelli, P. (2010). Assessing the relative contributions of transport efficiency and scavenging to seasonal variability in arctic aerosol. *Tellus B: Chemical and Physical Meteorology*, *62*(3), 190–196. https://doi.org/10.1111/j.1600-0889.2010.00453.x

Giglio, L., Randerson, J. T., van der Werf, G. R., Kasibhatla, P. S., Collatz, G. J., Morton, D. C., & DeFries, R. S. (2010). Assessing variability and long-term trends in burned area by merging multiple satellite fire products. *Biogeosciences*, *7*(3), 1171–1186. https://doi.org/10.5194/bg-7-1171-2010

Guenther, A., Karl, T., Harley, P., Wiedinmyer, C., Palmer, P. I., & Geron, C. (2006). Estimates of global terrestrial isoprene emissions using MEGAN (model of missions of gases and aerosols from nature). *Atmospheric Chemistry and Physics*, *6*(11), 3181–3210. https://doi.org/10.5194/acp-6-3181-2006

Hu, Y., Winker, D., Vaughan, M., Lin, B., Omar, A., Trepte, C., et al. (2009). CALIPSO/CALIOP Cloud phase discrimination algorithm. *Journal of Atmospheric and Oceanic Technology*, *26*(11), 2293–2309. https://doi.org/10.1175/2009JTECHA1280.1

Hubanks, P., King, M., Platnick, S., & Pincus, R. (2018). MODIS atmosphere L3gridded product algorithm theoretical basis document no. atbd-mod-30 for level-3 global gridded atmosphere products (08_D3, 08_E3, 08_M3) and Users Guide (Tech. Rep. April). MD: Adnet Systems, Lanham.

Jeffery, C. a., & Austin, P. H. (1997). Homogeneous nucleation of supercooled water: Results from a new equation of state. *Journal of Geophysical Research*, *102*(D21), 25,269–25,279. https://doi.org/10.1029/97JD02243

Kay, J. E., & L'Ecuyer, T. (2013). Observational constraints on arctic ocean clouds and radiative fluxes during the early 21st century. *Journal of Geophysical Research: Atmospheres*, *118*, 7219–7236. https://doi.org/10.1002/jgrd.50489

Komurcu, M., Storelvmo, T., Tan, I., Lohmann, U., Yun, Y., Penner, J. E., et al. (2014). Intercomparison of the cloud water phase among global climate models. *Journal of Geophysical Research: Atmospheres*, *119*, 3372–3400. https://doi.org/10.1002/2013JD021119

Korolev, A., McFarquhar, G., Field, P. R., Franklin, C., Lawson, P., Wang, Z., et al. (2017). Mixed-phase clouds: Progress and challenges. *Meteorological Monographs*, *58*, 5.1–5.50. https://doi.org/10.1175/AMSMONOGRAPHS-D-17-0001.1

Kuhns, H., Knipping, E. M., & Vukovich, J. M. (2005). Development of a United States-Mexico emissions inventory for the big bend regional aerosol and visibility observational (BRAVO) study. *Journal of the Air & Waste Management Association*, *55*(5), 677–692. https://doi.org/10.1080/10473289.2005.10464648

Lamb, D., & Verlinde, J. (2011). *Physics and Chemistry of Clouds*. New York: Cambridge University Press.

Le Treut, H., & Li, Z.-X. (1991). Sensitivity of an atmospheric general circulation model to prescribed SST changes: Feedback effects associated with the simulation of cloud optical properties. *Climate Dynamics*, *5*(3), 175–187. https://doi.org/10.1007/BF00251808

Liu, Y., Key, J. R., Ackerman, S. A., Mace, G. G., & Zhang, Q. (2012). Arctic cloud macrophysical characteristics from Cloudsat and CALIPSO. *Remote Sensing of Environment*, *124*, 159–173. https://doi.org/10.1016/j.rse.2012.05.006

Longley, I., Inglis, D., Gallagher, M., Williams, P., Allan, J., & Coe, H. (2005). Using NOx and CO monitoring data to indicate fine aerosol number concentrations and emission factors in three UK conurbations. *Atmospheric Environment*, *39*(28), 5157–5169. https://doi.org/10.1016/j.atmosenv.2005.05.017

Mackie, A. R., Palmer, P. I., Barlow, J. M., Finch, D. P., Novelli, P., & Jaeglé, L. (2016). Reduced arctic air pollution due to decreasing european and north American emissions. *Journal of Geophysical Research: Atmospheres*, *121*, 8692–8700. https://doi.org/10.1002/2016JD024923

Marelle, L., Raut, J.-C., Thomas, J. L., Law, K. S., Quennehen, B., Ancellet, G., et al. (2015). Transport of anthropogenic and biomass burning aerosols from Europe to the arctic during spring 2008. *Atmospheric Chemistry and Physics*, *15*(7), 3831–3850. https://doi.org/10.5194/acp-15-3831-2015

Martin, M., Tritscher, T., Jurányi, Z., Heringa, M. F., Sierau, B., Weingartner, E., et al. (2013). Hygroscopic properties of fresh and aged wood burning particles. *Journal of Aerosol Science*, *56*, 15–29. https://doi.org/10.1016/j.jaerosci.2012.08.006

Mioche, G., Jourdan, O., Ceccaldi, M., & Delanoë, J. (2015). Variability of mixed-phase clouds in the arctic with a focus on the svalbard region: A study based on spaceborne active remote sensing. *Atmospheric Chemistry and Physics*, *15*(5), 2445–2461. https://doi.org/10.5194/acp-15-2445-2015

Monks, S. A., Arnold, S. R., & Chipperfield, M. P. (2012). Evidence for El Niño-Southern Oscillation (ENSO) influence on arctic CO interannual variability through biomass burning emissions. *Geophysical Research Letters*, *39*, L14804. https://doi.org/10.1029/2012GL052512

Monks, S. A., Arnold, S. R., Emmons, L. K., Law, K. S., Turquety, S., Duncan, B. N., et al. (2015). Multi-model study of chemical and physical controls on transport of anthropogenic and biomass burning pollution to the Arctic. *Atmospheric Chemistry and Physics*, *15*(6), 3575–3603. https://doi.org/10.5194/acp-15-3575-2015

Morrison, H., de Boer, G., Feingold, G., Harrington, J., Shupe, M. D., & Sulia, K. (2011). Resilience of persistent arctic mixed-phase clouds. *Nature Geoscience*, *5*(1), 11–17. https://doi.org/10.1038/ngeo1332

Mossop, S. C. (1976). Production of secondary ice particles during the growth of graupel by riming. *Quarterly Journal of the Royal Meteorological Society*, *102*(431), 45–57. https://doi.org/10.1002/qj.49710243104

Murray, B. J., O'Sullivan, D., Atkinson, J. D., & Webb, M. E. (2012). Ice nucleation by particles immersed in supercooled cloud droplets. *Chemical Society Reviews*, *41*(19), 6519. https://doi.org/10.1039/c2cs35200a

Myhre, G., Bellouin, N., Berglen, T. F., Berntsen, T. K., Boucher, O., Grini, A., et al. (2007). Comparison of the radiative properties and direct radiative effect of aerosols from a global aerosol model and remote sensing data over ocean. *Tellus B: Chemical and Physical Meteorology*, *59*(1), 115–129. https://doi.org/10.1111/j.1600-0889.2006.00238.x

Olivier, J. G., Bloos, J. P. J., Berdowski, J. J., Visschedijk, A. J., & Bouwman, A. F. (1999). A 1990 global emission inventory of anthropogenic sources of carbon monoxide on $1^\circ \times 1^\circ$ developed in the framework of EDGAR/GEIA. *Chemosphere - Global Change Science*, *1*(1-3), 1–17. https://doi.org/10.1016/S1465-9972(99)00019-7

Paris, J.-D., Stohl, A., Nédélec, P., Arshinov, M. Y., Panchenko, M. V., Shmargunov, V. P., et al. (2009). Wildfire smoke in the siberian arctic in summer: Source characterization and plume evolution from airborne measurements. *Atmospheric Chemistry and Physics*, *9*(23), 9315–9327. https://doi.org/10.5194/acp-9-9315-2009

Parrington, M., Palmer, P. I., Henze, D. K., Tarasick, D. W., Hyer, E. J., Owen, R. C., et al. (2012). The influence of boreal biomass burning emissions on the distribution of tropospheric ozone over North America and the North Atlantic during 2010. *Atmospheric Chemistry and Physics*, *12*(4), 2077–2098. https://doi.org/10.5194/acp-12-2077-2012

Platnick, S., King, M., Ackerman, S., Menzel, W., Baum, B., Riedi, J., & Frey, R. (2003). The MODIS cloud products: Algorithms and examples from terra. *IEEE Transactions on Geoscience and Remote Sensing*, *41*(2), 459–473. https://doi.org/10.1109/TGRS.2002.808301

Platnick, S., King, M. D., Meyer, K. G., Wind, G., Amarasinghe, N., Marchant, B., et al. (2014). MODIS cloud optical properties: User guide for the collection 6 level-2 mod06/myd06 product and associated level-3 datasets (Tech. rep.). Washington: National Aeronautics and Space Administration.

Platnick, S., Pincus, R., Wind, B., King, M. D., Gray, M. A., & Hubanks, P. (2004). An initial analysis of the pixel-level uncertainties in global MODIS cloud optical thickness and effective particle size retrievals. *Proceedings of SPIE*, *5652*, 30–40. https://doi.org/10.1117/12.578353 December 2004.

Prenni, A. J., DeMott, P. J., Sullivan, A. P., Sullivan, R. C., Kreidenweis, S. M., & Rogers, D. C. (2012). Biomass burning as a potential source for atmospheric ice nuclei: Western wildfires and prescribed burns. *Geophysical Research Letters*, *39*, L11805. https://doi.org/10.1029/2012GL051915

Pruppacher, H. R. (1995). A new look at homogeneous ice nucleation in supercooled water drops. *Journal of the Atmospheric Sciences*, *52*(11), 1924–1933. https://doi.org/10.1175/1520-0469(1995)052<1924:ANLAHI>2.0.CO;2

Pruppacher, H., & Klett, J. (2010). *Microphysics of Clouds and Precipitation, Atmospheric and Oceanographic Sciences Library* (Vol. 18). Dordrecht: Springer Netherlands. https://doi.org/10.1007/978-0-306-48100-0

Rangno, A. L., & Hobbs, P. V. (2001). Ice particles in stratiform clouds in the Arctic and possible mechanisms for the production of high ice concentrations. *Journal of Geophysical Research*, *106*(D14), 15,065–15,075. https://doi.org/10.1029/2000JD900286

Riedi, J., Marchant, B., Platnick, S., Baum, B. A., Thieuleux, F., Oudard, C., et al. (2010). Cloud thermodynamic phase inferred from merged POLDER and MODIS data. *Atmospheric Chemistry and Physics*, *10*(23), 11,851–11,865. https://doi.org/10.5194/acp-10-11851-2010

Rosenfeld, D., Yu, X., Liu, G., Xu, X., Zhu, Y., Yue, Z., et al. (2011). Glaciation temperatures of convective clouds ingesting desert dust, air pollution and smoke from forest fires. *Geophysical Research Letters*, *38*, L21804. https://doi.org/10.1029/2011GL049423

Shaw, G. E. (1995). The arctic haze phenomenon. *Bulletin of the American Meteorological Society*, *76*(12), 2403–2413. https://doi.org/10.1175/1520-0477(1995)076<2403:TAHP>2.0.CO;2

Shupe, M. D. (2011). Clouds at arctic atmospheric observatories. Part II: Thermodynamic phase characteristics. *Journal of Applied Meteorology and Climatology*, *50*(3), 645–661. https://doi.org/10.1175/2010JAMC2468.1

Smoydzin, L., Teller, A., Tost, H., Fnais, M., & Lelieveld, J. (2012). Impact of mineral dust on cloud formation in a saharan outflow region. *Atmospheric Chemistry and Physics*, *12*(23), 11,383–11,393. https://doi.org/10.5194/acp-12-11383-2012

Stein, O., Schultz, M., Flemming, J., Inness, A., Kaiser, J., Jones, L., et al. (2011). MACC global air quality services—Technical documentation (Tech. rep.). Forschungszentrum Julich: MACC Global Air Quality Services.

Stephens, G. L. (2005). Cloud feedbacks in the climate system: A critical review. *Journal of Climate*, *18*(2), 237–273. https://doi.org/10.1175/JCLI-3243.1

Stohl, A., Forster, C., Huntrieser, H., Mannstein, H., McMillan, W. W., Petzold, A., et al. (2007). Aircraft measurements over Europe of an air pollution plume from Southeast Asia—Aerosol and chemical characterization. *Atmospheric Chemistry and Physics*, *7*(3), 913–937. https://doi.org/10.5194/acp-7-913-2007

Streets, D. G., Bond, T. C., Carmichael, G. R., Fernandes, S. D., Fu, Q., He, D., et al. (2003). An inventory of gaseous and primary aerosol emissions in Asia in the year 2000. *Journal of Geophysical Research*, *108*(D21), 8809. https://doi.org/10.1029/2002JD003093

Sun, J., Angal, A., Xiong, X., Chen, H., Geng, X., Wu, A., et al. (2012). MODIS reflective solar bands calibration improvements in collection 6. In H. Shimoda, X. Xiong, C. Cao, X. Gu, C. Kim, & A. S. Kiran Kumar (Eds.), *Proceedings of the SPIE* (Vol. 8528, pp. 85280N). Kyoto, Japan: Earth Observing Missions and Sensors: Development, Implementation, and Characterization II. https://doi.org/10.1117/12.979733

Tietze, K., Riedi, J., Stohl, A., & Garrett, T. J. (2011). Space-based evaluation of interactions between aerosols and low-level arctic clouds during the spring and summer of 2008. *Atmospheric Chemistry and Physics*, *11*(7), 3359–3373. https://doi.org/10.5194/acp-11-3359-2011

Uchiyama, A., Yamazaki, A., Shiobara, M., & Kobayashi, H. (2014). Case study on microphysical properties of boundary layer mixed-phase cloud observed at Ny-Ålesund, Svalbard: Observed cloud microphysics and calculated optical properties on 9 June 2011. *Polar Science*, *8*(2), 57–72. https://doi.org/10.1016/j.polar.2013.11.001

Vestreng, V., & Klein, H. (2002). Emission data reported to UNECE/EMEP. Quality assurance and trend analysis and presentation of WebDab (Tech. Rep.) Oslo, Norway: Norwegian Meteorological Institute.

Warneke, C., Bahreini, R., Brioude, J., Brock, C. a., de Gouw, J. A., Fahey, D. W., et al. (2009). Biomass burning in Siberia and Kazakhstan as an important source for haze over the Alaskan arctic in april 2008. *Geophysical Research Letters*, *36*, L02813. https://doi.org/10.1029/2008GL036194

Xie, Y. (1999). Identification of source nature and seasonal variations of arctic aerosol by the multilinear engine. *Atmospheric Environment*, *33*(16), 2549–2562. https://doi.org/10.1016/S1352-2310(98)00196-4

Yang, Q., Easter, R. C., Campuzano-Jost, P., Jimenez, J. L., Fast, J. D., Ghan, S. J., et al. (2015). Aerosol transport and wet scavenging in deep convective clouds: A case study and model evaluation using a multiple passive tracer analysis approach. *Journal of Geophysical Research: Atmospheres*, *120*, 8448–8468. https://doi.org/10.1002/2015JD023647

Zamora, L. M., Kahn, R. a., Cubison, M. J., Diskin, G. S., Jimenez, J. L., Kondo, Y., et al. (2016). Aircraft-measured indirect cloud effects from biomass burning smoke in the arctic and subarctic. *Atmospheric Chemistry and Physics*, *16*(2), 715–738. https://doi.org/10.5194/acp-16-715-2016

Zamora, L. M., Kahn, R. A., Huebert, K. B., Stohl, A., & Eckhardt, S. (2018). A satellite-based estimate of aerosol-cloud microphysical effects over the arctic ocean. *Atmospheric Chemistry and Physics Discussions*, 1–22. https://doi.org/10.5194/acp-2018-514